

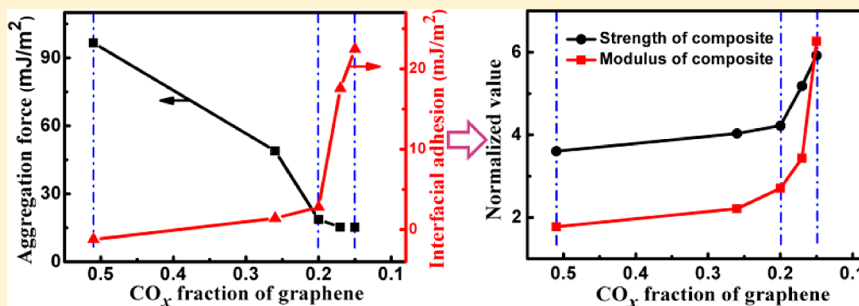
Rational Design of Graphene Surface Chemistry for High-Performance Rubber/Graphene Composites

Zhenghai Tang,[†] Liqun Zhang,[‡] Wenjiang Feng,[†] Baochun Guo,*[†] Fang Liu,[†] and Demin Jia[†]

[†]Department of Polymer Materials and Engineering, South China University of Technology, Guangzhou 510640, P. R. China

[‡]State Key Laboratory of Organic/Inorganic Composites, Beijing University of Chemical Technology, Beijing 100029, P. R. China

S Supporting Information



ABSTRACT: In a rubber/filler composite, the surface chemistry of the filler is a critical factor in determining the properties of the composite because it affects the dispersion of the filler and the interfacial adhesion between the filler and rubber. In this study, we primarily focus on how graphene surface chemistry affects the dispersion of graphene and interfacial adhesion in butadiene–styrene rubber (SBR)/graphene composites and on the resultant properties of the composites. Composites that contain graphene with tailored surface chemistry are prepared via the chemical reduction of graphene oxide (GO) *in situ*. Subsequently, the dispersion of the graphene and interfacial adhesion are fully investigated in relation to the graphene surface chemistry. As revealed by dielectric relaxation spectroscopy, the bulk segmental relaxation is independent of the graphene surface chemistry, whereas the interfacial relaxation mode is retarded in the composite with stronger graphene–rubber affinity. The contribution of the graphene surface chemistry to the dispersion of the graphene and interfacial adhesion is quantified by calculating the surface energies. The results indicate that, when the CO_x fraction in the graphene is greater than 0.2, it exerts an increasingly strong effect on the dispersion of the graphene; in contrast, when the CO_x fraction is less than 0.2, it exerts a significant and positive effect on the interfacial interaction. In particular, on the basis of the surface energy analysis, quantitative predictors for the dispersion of graphene and interfacial adhesion are presented; these predictors can be used for the virtual design of graphene surface chemistry to optimize the properties of composites.

1. INTRODUCTION

Rubbers are acknowledged to be strategically important materials, and the reinforcement of rubbers through the incorporation of nanosized fillers is essential because most neat rubbers are mechanically weak. Carbon black and silica are conventional fillers that are widely used in the rubber industry. The dispersion of the filler and filler–rubber interactions are generally acknowledged to be two key factors that govern the properties of the final composites, and these factors are known to strongly depend on the surface chemistry of the filler.^{1,2} Collectively, the optimization of the surface chemistry of the filler is beneficial for strengthening the interfacial adhesion and improving the filler dispersion and consequently enhancing the overall performances of the composites.^{3,4}

Graphene, a single-atom-thick sheet of carbon atoms densely packed in a honeycomb crystal lattice, has been the subject of considerable interest and study because of its intriguing and outstanding physical properties.⁵ As expected, graphene holds promising applications in rubber composites by virtue of its

potential to efficiently endow rubber with reinforcement and functional properties at very low loading.^{6,7} As noted above, to maximize the reinforcing efficiency of graphene in rubber composites, it is critically important, but often challenging, to optimize the surface chemistry of the graphene to improve its dispersion and enhance the interfacial interaction between the graphene and rubber matrix. To date, considerable effort has been devoted to the functionalization of graphene and preparation of graphene derivatives. For example, pristine graphene is defect-free and inert; therefore, it shows poor compatibility with most polymer matrices and tends to severely aggregate in composites. As a result, pristine graphene is typically unsuitable for use as polymer reinforcement.^{8,9} Alternatively, graphene oxide (GO), a versatile precursor for the preparation of graphene, has been extensively studied for

Received: October 29, 2014

Revised: December 1, 2014

Published: December 5, 2014

use as filler in place of pristine graphene.¹⁰ Because GO contains abundant oxygenic groups introduced by an oxidization reaction, it exhibits superior reinforcing efficiency for polar rubbers such as carboxylated acrylonitrile–butadiene rubber¹¹ and nitrile rubber¹² because the oxygen-containing groups present on GO sheets are in favor of strengthening the interfacial interaction. Moreover, the oxidative debris on GO sheets has been observed to play a critical role in both dispersing GO and ensuring interfacial stress transfer in composites.¹³ However, GO has limited compatibility with most nonpolar rubbers because of its hydrophilic nature. For the preparation of nonpolar rubber/GO composites, the surface modification of GO is essential. For example, Liu et al. utilized butadiene–styrene–vinylpyridine rubber as an interface bridge between GO and SBR to improve their compatibility.¹⁴ Huang et al. used silane-modified GO as a multifunctional filler for natural rubber (NR).¹⁵ Other graphene derivatives, such as thermally or chemically reduced graphene, have also been incorporated into rubbers to enhance their properties. For instance, Hernandez et al. prepared NR/thermally reduced graphene composites by conventional two-roll mill mixing.¹⁶ Zhan et al. incorporated chemically reduced graphene into NR by an ultrasonically assisted latex mixing and *in situ* reduction of GO.¹⁷ Upon reduction, most oxygenic groups are removed from GO; however, some defects that can serve as active sites still remain, leading to increased interaction between the graphene and rubber.¹⁸ As a consequence, compared with GO, reduced graphene exhibits much higher reinforcing efficiency for nonpolar rubbers.

However, in spite of these efforts, several key fundamental issues have not yet been fully addressed. For instance, how does the graphene surface chemistry affect the graphene–rubber interphase and graphene dispersion? What is the ideal or optimized surface chemistry of graphene for rubber reinforcement?

In the present work, we prepared SBR/graphene composites filled with graphene with tailored surface chemistry and subsequently investigated the influences of graphene surface chemistry on the dispersion, interfacial adhesion, and the final properties of the composites. Dielectric relaxation spectroscopy provides significant insights into the effects of the graphene surface chemistry on the dynamics of the composites at the molecular level. The contributions of graphene surface chemistry to the dispersibility and interfacial adhesion are quantitatively determined using surface energy.

2. EXPERIMENTAL SECTION

Materials. SBR latex (Intex 132, solid content of 66 wt %, styrene content of 25%) was manufactured by Polimeri Europa, Italy. Graphite powder (size <20 µm, purity >99.8%) was purchased from Shanghai Colloidal Co. Ltd. Hydrazine hydrate (80%) and glycerol were obtained from Tianjin Fuyu Fine Chemical Co. Ltd. The reagents used for the oxidation of the graphite, including concentrated sulfuric acid, potassium permanganate, and sodium nitrate, were analytically pure. All the rubber ingredients were industrial grade and used as received.

Preparation of SBR Composites. Graphite oxide was prepared by oxidizing natural graphite based on a modified Hummers method, following our previous work.¹⁹ The obtained graphite oxide was exfoliated in deionized water under sonication to form 2 mg/mL GO aqueous dispersion. Then, a desired amount of the GO dispersion was added into SBR latex and stirred for 2 h, and the GO content was controlled to be 1, 3, 5, or 7 phr (parts per one hundred parts of gum). The mixture was subsequently coagulated by adding calcium chloride aqueous solution (1.0 wt %) as the flocculating agent to

obtain SBR/GO compounds. To prepare SBR/graphene (SBR/G) compounds, hydrazine hydrate (20 times weight relative to GO) was added into the coagulated SBR/GO compound suspensions to reduce the GO, and the reduction was maintained at 95 °C for 10 h. It should be noted that hydrazine hydrate cannot react with SBR in the absence of catalysts, as evidenced by the FTIR spectra (Figure S1). Finally, the resulting SBR/GO and SBR/G compounds were washed with abundant deionized water, followed by vacuum drying at 50 °C overnight.

The dried compounds were compounded with the ingredients using a two-roll mill and subjected to compression at 150 °C for the optimum curing time, as determined using a vulcameter. The basic formulation of the composite was as follows: SBR 100 g; zinc oxide 5 g; stearic acid 1 g; dibenzothiazole disulfide 1.5 g; *N*-cyclohexyl-2-benzothiazole 1 g; sulfur 1.5 g. In this context, the abbreviation of SBR/GO(x) represents the composite filled with x phr of GO, and the notation of SBR/G(x) represents the composite containing x phr of reduced graphene (reduction with 20 times more hydrazine hydrate than GO by weight at 95 °C for 10 h). It should be noted that the actual graphene contents in SBR/G(x) composites is lower than the value of x because the reduction of the GO leads to a loss of weight of GO.

A series of SBR/graphene composites with tailored reduction extent and surface chemistry were also prepared from SBR/GO compounds by controlling the reduction conditions, including the reducer type and dosage, reduction temperature, and time. Typically, the SBR/GO₃ compound was subjected to slight reduction with a 1:1 hydrazine hydrate ratio relative to the GO content at 80 °C for 1 h (sample code SBR/G₃-T80), to moderate reduction with a 10:1 hydrazine hydrate ratio at 90 °C for 4 h (sample code SBR/G₃-T90), to typical reduction with a 20:1 hydrazine hydrate ratio at 95 °C for 10 h (sample code SBR/G₃, as noted above), and to severe reduction and simultaneous N-doping with a 20:1 hydrazine hydrate ratio and a 20:1 ammonia ratio at 95 °C for 10 h (sample code SBR/GN₃-T95). All preparation processes were performed according to the aforementioned protocols.

Preparation of Graphene Samples. To study the graphene surface properties and eliminate any confounding influence of the SBR matrix, graphene samples with tailored reduction extent were synthesized via direct reduction of GO aqueous dispersion using the previously described reduction conditions. The samples that were thus reduced using a 1:1 hydrazine hydrate ratio at 80 °C for 1 h, a 10:1 hydrazine hydrate ratio at 90 °C for 4 h, a 20:1 hydrazine hydrate ratio at 95 °C for 10 h, and a 20:1 hydrazine hydrate ratio and a 20:1 ammonia ratio at 95 °C for 10 h were coded as G₈₀, G₉₀, G₉₅, and GN₉₅, respectively. After reduction, the samples were washed with deionized water and subjected to freeze-drying to obtain graphene powders.

Characterizations. X-ray spectroscopy (XPS) analysis was carried out on a Kratos Axis Ultra DLD equipped with Al K α radiation source (1486.6 eV). Raman spectroscopy was collected by LabRAM Aramis of HO RIBA Jobin Yvon, which was equipped with a He–Ne ion laser (532.0 nm) as an excitation source. The curing characteristics were determined at 150 °C using a U-CAN UR-2030 vulcameter. Dynamic mechanical analysis (DMA) was performed on a TA DMA Q800 instrument under a tensile mode with a dynamic strain of 0.5%. The samples were scanned from –80 to 80 °C, and the frequency and heating rate were fixed at 5 Hz and 3 °C/min, respectively. Transmission electron microscopy (TEM) for the ultramicrotomed samples was conducted on Tecnai G2 F30 S-Twin electron microscope operated at an accelerating voltage of 30 kV. The cryogenically fractured surfaces of the composites were observed using field-emission scanning electron microscopy (SEM, Hitachi S-4800, Japan). Swelling experiments were performed by immersing vulcanizates in toluene at room temperature, and then the volume fraction of the rubber in the swollen rubber (V_r) was determined. The detailed calculation procedures are described elsewhere.²⁰ Tensile tests were performed on U-CAN UT-2060 following ISO 37-2005. To ensure data accuracy and repeatability, six specimens were measured for each sample, and the average value was given. Dielectric relaxation measurements were conducted on an ALPHA-ANB broadband

dielectric/impedance spectrometer (Novocontrol Technologies GmbH, Hundsangen, Germany). Vulcanized composite samples with a thickness of ~2 mm were placed between two parallel gold-plated electrodes of 20 mm in diameter. Measurements were carried out over the frequency window of 10^{-1} – 10^6 Hz in the temperature range from –100 to +100 °C in steps of 5 °C. Static contact angles were measured using the Krüss DSA100 drop shape analysis system (Krüss GmbH, Germany). The contact angle was recorded within 2 s after liquid deposition. Water and glycerol were used as the test liquids. To prepare the samples for the contact angle measurements, graphene powders were pressed into thin disks using a powder tablet press, and SBR was dissolved in toluene, coated onto a glass slide, and then dried to form a film.

3. RESULTS AND DISCUSSION

Variation in Surface Chemistry of Graphene. XPS measurements were performed to quantitatively study the surface chemistry of the GO and graphene samples with different reduction extents. The XPS survey scans and C 1s XPS spectra for the GO and graphene samples are presented in Figure S2, and the results of the XPS analysis are summarized in Table 1. GO exhibits a considerable degree of oxidation with

Table 1. XPS Analysis Results for the Surface Chemistry of GO and Graphene

sample	CO _x fraction	C=C fraction	C–N fraction	(C=C) + (C–N) fraction
GO	0.51	0.49	0	0.49
G ₈₀	0.26	0.62	0.12	0.74
G ₉₀	0.20	0.68	0.12	0.80
G ₉₅	0.17	0.65	0.18	0.83
GN ₉₅	0.15	0.60	0.25	0.85

four types of carbon atoms including C=C (284.8 eV), C–O (286.8 eV), C=O (287.5 eV), and O–C=O (289.1 eV). Moreover, the fraction of oxygenic carbon atoms (CO_x, the area of the peaks associated with oxygen-containing functional groups divided by the total area) in GO is established to be 0.51. Upon reduction, although the C 1s XPS spectra of the graphene exhibit the same oxygen-containing functional groups as those of the GO, the CO_x fraction of graphene monotonically decreases as the reduction extent deepens. Accordingly, the C=C fraction of the graphene samples is sharply increased, referring to GO. However, the C=C fraction is insensitive to the reduction extent, as evidenced by the slight variation in the C=C fraction from G₈₀ to GN₉₅. In addition, an additional component corresponding to C–N (285.4 eV) is present in the resulting graphene, and the C–N fraction gradually increases and reaches the highest value in GN₉₅. In previous studies, a similar N-doping effect has also been observed in hydrazine–hydrate-reduced graphene, and the doping level has been observed to be greatly increased in the presence of ammonia.^{21,22}

Raman spectroscopy is a powerful and convenient tool for the investigation of the structures of carbonaceous materials, especially for distinguishing ordered and disordered structures. The structural evolution of graphene during the reduction process was investigated by Raman spectroscopy. As shown in Figure 1, two prominent peaks corresponding to the G and D bands are observed in all of the spectra. In general, the intensity ratio of the D to G bands ($I(D/G)$) is inversely proportional to the average size of the sp² domains.²³ Compared with that of GO, the $I(D/G)$ of graphene is considerably increased,

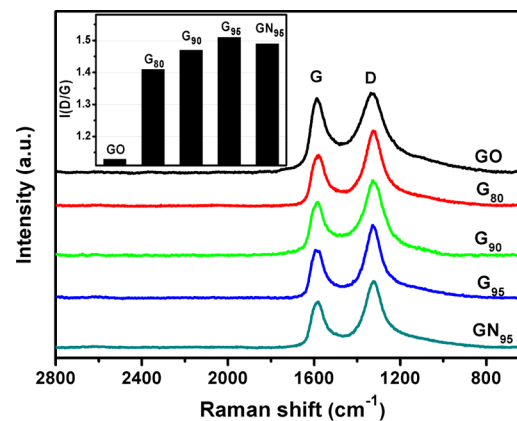


Figure 1. Raman spectra of GO and graphene samples.

indicating that more sp² domains with smaller sizes are formed during reduction.²⁴ However, the $I(D/G)$ values for all graphene samples are almost invariant, suggesting that the microcrystallite structure of the graphene is unchanged, which is well consistent with the XPS results that indicate the minimal variation in C=C fraction among the graphene samples.

Dispersion of Fillers and Interfacial Adhesion in Composites. In polymer composites, the dispersion of the filler and interfacial interactions are critical to the properties of the composites. In this study, the dispersion status of the fillers was first evaluated by TEM measurements. Figure 2 compares

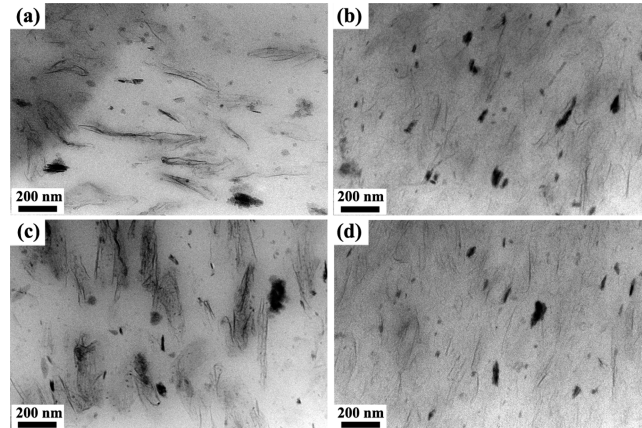


Figure 2. TEM images of (a) SBR/GO3, (b) SBR/G3, (c) SBR/GO7, and (d) SBR/G7 composites.

the dispersion of the fillers, for example, GO and G₉₅, in the SBR matrix. As shown in Figures 2a and 2c, obvious GO aggregation is observed in SBR/GO3 and SBR/GO7 composites. This is because the GO sheets bear abundant oxygenic groups, causing GO to have poor polarity matching and poor compatibility with the nonpolar SBR. In striking contrast, as shown in Figures 2b and 2d, the graphene are uniform dispersed throughout the matrix without aggregation, manifesting the superior compatibility between graphene and SBR. As described in the Experimental Section, SBR/graphene compounds were produced by the reduction of cocomagulated SBR/GO compounds *in situ*; therefore, the initial dispersion status of the GO or graphene in each compound is identical. Evidently, the distinct difference in dispersion status between GO and graphene is originated from the difference in the wettability of the filler by SBR during milling and from the

reaggregation of the filler during the hot-pressing process (as discussed below). Considering that the difference in atomic number between graphene and SBR is very low, it is difficult to definitely quantify the dispersion status of graphene through TEM measurement, and a similar dilemma has also been reported in other studies.²⁵ Therefore, the TEM images of the SBR/graphene composites containing graphene with other reduction extents are not present.

To investigate the morphology of the composites, SEM measurements were performed on the cryofractured surfaces. Figure 3 highlights the difference between GO and G₉₅.

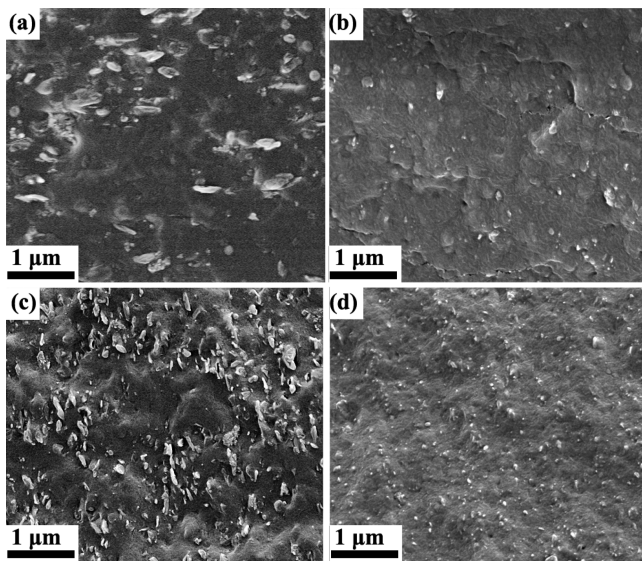


Figure 3. SEM images of (a) SBR/GO3, (b) SBR/G3, (c) SBR/GO7, and (d) SBR/G7 composites.

dispersed in SBR. In the SEM image of the SBR/GO3 composite (Figure 3a), numerous GO sheets are clearly observed to have pulled out of the matrix, evidencing poor adhesion between GO and SBR. In the case of SBR/GO7, more sheets are extracted from the matrix with increasing GO loading (Figure 3c). As shown in Figures 3b and 3d, the fractured surfaces of SBR/G3 and SBR/G7 exhibit distinctly different characteristics. Graphene sheets are uniform dispersed throughout the composites without extraction, and the interface between the graphene and SBR is very blurry because of the embedding of graphene sheets into the matrix. SEM images of

SBR/G3-T80 and SBR/G3-T90 were examined (Figure S3). The number of protuberances on the fractured surfaces gradually decreases as the CO_x fraction of graphene decreases with respect to SBR/GO3. A comparison of the SEM images of SBR/G05 and SBR/G5 also reveals similar phenomena (Figure S3). All of these observations provide evidence that the interfacial interaction between graphene and SBR is superior to that between GO and SBR.

To further evaluate the influence of the graphene surface chemistry on the interfacial adhesion and dispersion in the composites, equilibrium swelling experiments and DMA analysis were performed. In the swelling measurements, the ratio of V_{r0} to V_{rf} (V_{r0}/V_{rf}) represents the degree of restriction on the swelling of the rubber matrix that is exerted by the interaction between the rubber and filler, where V_{r0} and V_{rf} are the volume fractions of rubber in unfilled and filled vulcanized samples, respectively, after swelling.^{26,27} Any or all factors, including filler dispersion and concentration, interface, and barrier effects, may affect the swelling. However, in the swelling experiment, because equilibrium swelling of the composite is achieved and the effect of the filler loading on the swelling is excluded, the barrier effects caused by the graphene are not relevant, and thus the V_{r0}/V_{rf} is mainly dependent on the graphene dispersion and interfacial interaction.²⁶ Figure 4a presents the dependence of V_{r0}/V_{rf} on the filler loading and on the graphene surface chemistry. In both SBR/GO and SBR/G composites, V_{r0}/V_{rf} gradually decreases as the filler loading increases. This behavior can be explained by the fact that the mobility of the rubber chains near the filler is restricted by the attachment of the rubber segments to the filler surfaces; thus, the rubber surrounding the filler exhibits diminished swelling ability.²⁷ In addition, the strong interfacial interactions may cause geometrical constraints at the SBR/graphene interface, which also accounts for the decreased swelling of the polymer network.²⁸ Compared with the V_{r0}/V_{rf} value for the SBR/GO composite, that for the SBR/G composite at the same filler loading is much lower. Furthermore, when the filler loading is 3 phr, V_{r0}/V_{rf} monotonically decreases as the CO_x fraction of the graphene decreases. The decreasing V_{r0}/V_{rf} of the composites is attributed to the fact that the stronger interfacial interaction and better dispersion of the graphene effectively prevent the diffusion of solvent molecules into the interphase.

In Figure 4b, the tan δ values of the composites containing 3 phr filler are plotted against temperature. The glass transition temperature of the composites determined at the maximum value of the tan δ is almost unchanged, implying that the

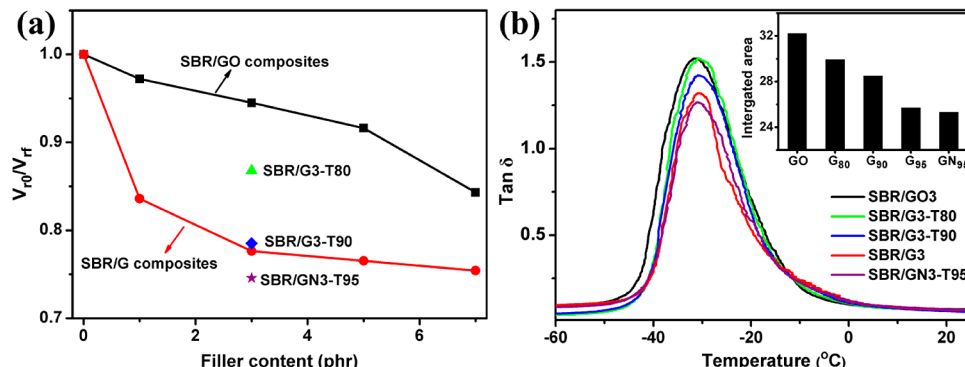


Figure 4. (a) Dependence of V_{r0}/V_{rf} on filler content and graphene surface chemistry. (b) Tan δ of the composites containing 3 phr filler as a function of temperature. The inset is the integrated area of the peak of tan δ.

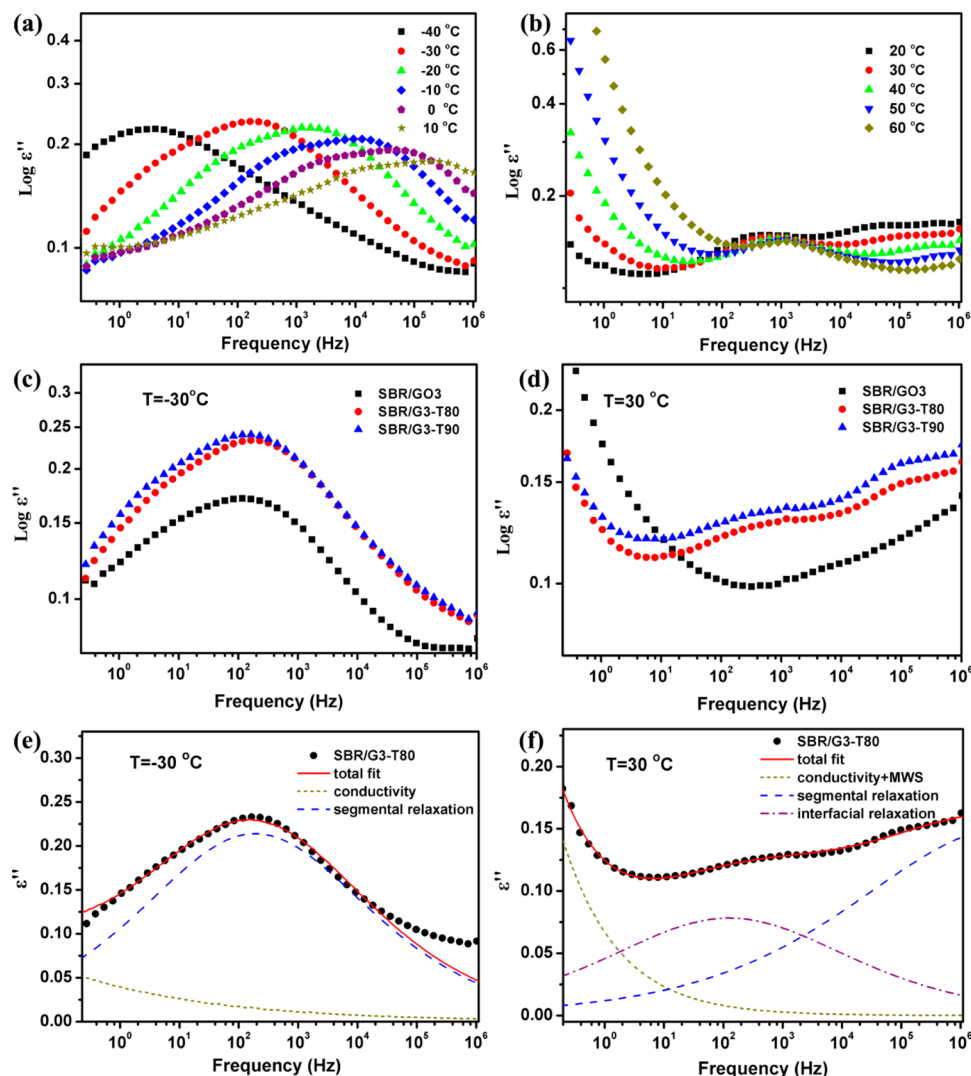


Figure 5. Dielectric loss ϵ'' of SBR/G3-T80 as a function of frequency at temperatures ranging from (a) -40 to 10 °C and from (b) 20 to 60 °C. Comparison on the selected dielectric loss spectra (c) at -30 °C and (d) at 30 °C for the SBR/GO3, SBR/G3-T80, and SBR/G3-T90 composites. Deconvolutions of the dielectric loss spectra at (e) -30 °C and (f) 30 °C for the SBR/G3-T80 composite; the spectra were deconvoluted using the HN function.

relaxation of bulk segments is not influenced by adding GO or graphene. It is consistent with the observations from dielectric relaxation measurement (will be discussed below). Notably, the maximum value of $\tan \delta$ and its integrated area of the composites are monotonically decreased with decreasing CO_x fraction of the graphene. The significantly suppressed maximum value of $\tan \delta$ is apparently related to the larger modulus of the composites (will be discussed below). Considering that the filler content is the same, the decreased peak value and peak area of $\tan \delta$ are related to the reduced fraction of the bulk matrix, which is caused by the adsorption of rubber chain onto the sheet surface to form the interfacial region. The consistently increased interphase fraction (hence the consistently decreased bulk fraction) is attributed to the improved interfacial bonding and dispersion of graphene. As for example, the use of silane coupling agent in silica-filled rubber composite led to a reduction in $\tan \delta$ peak height due to the improved interfacial adhesion and dispersion of silica.²⁹ It needs to point out that the interfacial relaxation of the immobilized rubber at graphene-SBR interfaces cannot be resolved on the high temperature side in the $\tan \delta$ curves, which may be due to

its low sensitivity in probing the viscoelastic behavior at molecular level^{30,31}

The dispersion status of the filler and the filler-rubber interfacial interaction is also reflected by the minimum torque (ML) and maximum torque (MH) of the composites, as measured during curing. ML and MH are well documented to predominantly depend on the filler network, the rubber network, and the rubber-filler interactions.^{32,33} As evidence of the validity of this claim, as shown in Figure S4, ML and MH are remarkably increased with increasing filler loading; this behavior is ascribed to the formation of filler-filler network and filler-rubber interactions in the composites. Meanwhile, for a constant filler content, the ML and MH values for SBR/G composites are always much higher than those for SBR/GO composites, and ML and MH tend to increase as the CO_x fraction of the graphene increases. This behavior is indicative of the improved dispersion of the graphene and enhanced interfacial interaction that arise upon the reduction of GO.^{33,34}

Dielectric Relaxation Spectroscopy Study of SBR Composites. Broadband dielectric spectroscopy (BDS) is a powerful tool for studying polymer dynamics through

measuring the dipolar relaxation of a polymer under an electric field over different time scales. In this study, BDS was used to investigate the effect of the graphene surface chemistry on the polymer relaxation and the interfacial structure of the composites at the molecular level. Figure 5a presents the dielectric relaxation as a function of frequency for SBR/G3-T80 at temperatures ranging from -40 to 10 °C. In each spectrum, a clear loss peak associated with bulk segment relaxation is observed, and this peak shifts toward higher frequencies with increasing temperature, which is well-known to be a thermally activated process. A comparison of selected dielectric loss spectra for the composites at -30 °C is displayed in Figure 5c. All of the composites exhibit similar profiles, indicating that the surface chemistry of the graphene may have little effect on the bulk relaxation process. Furthermore, the dielectric loss spectra were fitted to the Havriliak–Negami (HN) function.³⁵ Figure 5e is the typical fitting for the dielectric loss data of SBR/G3-T80 at -30 °C using the HN function with a conductivity term arising from ionic conductivity of impurities. A characteristic relaxation time, τ_{\max} , obtained from the HN fit can be correlated with the temperature through the Vogel–Fulcher–Tamman (VFT) equation:³⁵

$$\tau_{\max} = \tau_0 \exp\left(\frac{B}{T - T_0}\right) \quad (1)$$

where τ_0 , B , and T_0 are constants. Figure 6 shows τ_{\max} plotted as a function of inverse temperature for the composites. The

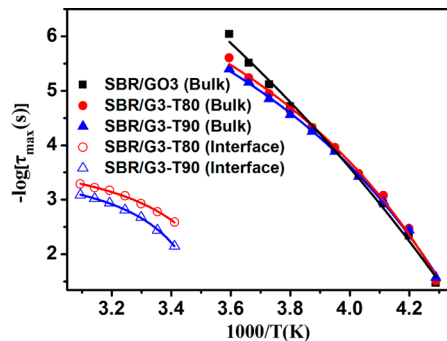


Figure 6. Bulk and interfacial relaxation times as functions of temperature for SBR/GO3, SBR/G3-T80, and SBR/G3-T90. The solid lines are the fits to the data using the VFT equation.

glass transition temperature is conventionally determined by extrapolating the VFT fit to the temperature at which the relaxation time, τ_{\max} , is 100 s.^{35,36} In this manner, the bulk glass transition temperature (T_{bg}) for all composites was calculated to be approximately -60.0 °C, further confirming that the bulk segmental relaxation is not affected by the graphene surface chemistry.

The dielectric loss spectra of SBR/G3-T80 composite at higher temperatures ranging from 20 to 60 °C are shown in Figure 5b. At such temperature window, the dielectric loss value at low frequency is sharply increased, which may be due to the combination effects of the conductivity and Maxwell–Wagner–Sillars (MWS, or interfacial polarization). The effects are more pronounced with increasing temperature. Such a phenomenon has also been reported by others.^{37–39} Interestingly, an additional relaxation, which is slower than bulk polymer relaxation, is clearly observed in the frequency range of 10^2 – 10^4 Hz. SBR/G3-T90 also exhibits the slower relaxation peak,

whereas this relaxation mode is absent in SBR/GO3 (Figure 5d). These findings are reminiscent of similar observations in clay-based rubber composites. Giannelis et al. have observed a slower interfacial relaxation in SBR/clay composites, whereas the interfacial mode was too weak to analyze in SBR/silica and SBR/carbon black composites.³⁵ Moreover, Hernandez et al. observed a new relaxation mode (interfacial relaxation) in organoclay filled NR composites, whereas this relaxation mode was absent in the corresponding unmodified-clay filled NR composites with poorer intercalation.³⁸ It is commonly admitted that the interfacial relaxation is related to the restricted mobility of the polymer chains at the filler–rubber interface, which predominantly depends on the interfacial strength and exfoliation status of the fillers. In this study, the slower relaxation observed in SBR/G3-T80 and SBR/G3-T90 is attributed to the restricted motion of the SBR chains imposed by the graphene. By contrast, in SBR/GO3, the SBR chains are less confined by the GO because of their weak interfacial adhesion; therefore, the signal of the interfacial relaxation is too weak to detect. To distinguish the interfacial relaxation from MWS, the electric modulus formalism was employed to separately investigate the MWS relaxation by excluding the conductivity contribution at high temperature.^{38,40} The dielectric loss modulus of the SBR/G3-T80 is shown in Figure S5. It can be seen that the MWS appears at low frequency region from 10^{-1} to 10^2 Hz, which is much lower than that for the interfacial relaxation we mentioned. Besides, the intensity of the MWS is much higher than the polymer chain relaxation. Therefore, it is reasonable to conclude that the slower relaxation process is related to the restricted polymer chains at graphene/SBR interface.

Figure 5f presents the dielectric loss spectrum for SBR/G3-T80 at 30 °C fitted using the sum of two HN relaxation processes (specifically, interfacial and segmental relaxations) and the combination relaxations of MWS and conductivity. Subsequently, the relaxation time τ_{\max} of the interfacial mode and temperature can be excellent fitted using the VFT equation with a correlation factor above 0.995 , as also illustrated in Figure 6. Compared with the bulk relaxation, the interfacial relaxation time is slower by several orders of magnitude. Furthermore, the interfacial glass transition temperature (T_{ig}) determined by extrapolating the VFT fit to the temperature at which τ_{\max} is 100 s, analogous to the calculation for the bulk case, is calculated to be -6.4 and 6.5 °C for SBR/G3-T80 and SBR/G3-T90, respectively; both values are much higher than T_{bg} (-60.0 °C). In a previous report, T_{ig} of SBR/clay composite was demonstrated to be approximately 80 °C higher than the T_{bg} .³⁵ In addition, compared with the interfacial relaxation time for SBR/G3-T80, that for SBR/G3-T90 is much slower, which suggests the presence of a stronger interfacial interaction in SBR/G3-T90 composite.

It should be noted that the dielectric loss peaks for SBR/G3 and SBR/GN3-T95 are completely obscured over the entire temperature region because the conductivity and MWS relaxation improves substantially as the reduction extent and dispersion of graphene increases (Figure S6). Similar observations have also been reported in other studies of conducting-filler-filled polymer composites.^{41,42} Therefore, the discussion on dielectric loss data for the SBR/G3 and SBR/GN3-T95 is not involved.

Quantitative Predictors for Dispersion and Interfacial Interaction in Composites. In rubber composites, the wettability of the filler by rubber, the interfacial adhesion

between filler and rubber, and the reagglomeration of filler in rubber are thermodynamically driven by the physicochemical surface properties of filler and rubber matrix. As reported by Heinrich and Natarajan, the thermodynamic contribution to the dispersibility and interfacial adhesion can be quantified in terms of surface energies.^{43,44} Herein, to gain insights into the effects of the graphene surface chemistry on the dispersion of graphene and interfacial adhesion in the composites, we use Fowkes' model to calculate the surface energies of the fillers and SBR matrix. In Fowkes' model, the surface energy can be split into a polar component and a dispersive component, and the surface energy of a solid can be evaluated by measuring the contact angles of two liquids, as described in eqs 2 and 3:⁴⁵

$$\gamma_L(1 + \cos \theta) = 2(\sqrt{\gamma_L^d \gamma_s^d} + \sqrt{\gamma_L^p \gamma_s^p}) \quad (2)$$

$$\gamma_s = \gamma_s^d + \gamma_s^p \quad (3)$$

where γ_L^p and γ_L^d are the polar and dispersive components, respectively, of the surface energies of the liquid; γ_s^p and γ_s^d are the polar and dispersive components, respectively, of the surface energies of the solid; and γ_L and γ_s are the total surface energies of the liquid and solid, respectively, expressed as the sum of the polar and dispersive components. The test liquids were water and glycerol. The γ_L^p and γ_L^d values for water are 51 and 21.8 mJ/m², respectively, and the γ_L^p and γ_L^d values for glycerol are 30 and 34 mJ/m², respectively. The surface energies of GO and graphene samples with different surface chemistry were calculated by substituting the contact angles and surface energies of the test liquids into eqs 2 and 3; the results are summarized in Table 2. The surface energy of GO is

Table 2. Surface Energies of GO, Graphene with Varied Reduction Extent, and SBR

sample	γ_s^d (mJ/m ²)	γ_s^p (mJ/m ²)	γ_s (mJ/m ²)
GO	0.0	64.7	64.7
G ₈₀	1.8	41.7	43.5
G ₉₀	5.9	23.8	29.7
G ₉₅	40.4	2.4	42.8
GN ₉₅	31.6	16.0	47.6
SBR	13.3	4.3	17.6

determined to be 64.7 mJ/m², which is close to the value of 62.1 mJ/m² reported by Wang et al.⁴⁶ GO has a high polar surface-energy component because it bears numerous oxygenic groups such as epoxides, hydroxyls, and carboxyls. Obviously,

compared with the γ_s^p value of GO, those of graphene samples (from G₈₀, G₉₀ to G₉₅) monotonically decrease with decreasing CO_x fraction. Given that the polar component is evoked by polar functional groups, the decrease in γ_s^p is apparently related to the removal of oxygen-containing groups. In addition, the γ_s^p of GN₉₅ is larger than that of G₉₅, which is attributable to the increased N-doping level in GN₉₅. The surface energy of SBR matrix is determined to be 17.6 mJ/m².

The wettability of the filler by rubber can be predicted by the ratio of the work of adhesion between the filler and rubber to the work of adhesion between the filler and filler (W_{RF}/W_{FF}), and the contact angle (θ) of rubber on filler surface can be expressed using eq 4:^{47,48}

$$\cos \theta = -1 + 2 \frac{\sqrt{\gamma_R^d \gamma_F^d} + \sqrt{\gamma_R^p \gamma_F^p}}{\gamma_F} = -1 + 2 \frac{W_{RF}}{W_{FF}} \quad (4)$$

where γ_F^p and γ_F^d are the polar and dispersive components of the surface energy of the filler, respectively; γ_R^p and γ_R^d are the polar and dispersive components of the surface energy of the rubber matrix, respectively; and γ_F is the total surface energy of the filler. When W_{RF}/W_{FF} is less than 1 ($\cos \theta < 1$), the attraction between the filler and rubber is lower than that between the filler and filler, suggesting that the filler will tend to agglomerate to lower the interfacial energy. When W_{RF}/W_{FF} is greater than or equal to 1 ($\cos \theta \geq 1$), the attraction between the filler and rubber is greater than or equal to that between the filler and filler, indicating that the filler can be easily wetted by the rubber. The values of $\cos \theta$ of SBR on GO and graphene surfaces are calculated and tabulated in Table S1. All the values of $\cos \theta$ are lower than 1, indicating that neither GO nor graphene can be well wetted by SBR due to the strong attraction between filler sheets. Compared with GO, the value of $\cos \theta$ constantly increases with decreasing CO_x fraction of the graphene, delivering a greater wettability between graphene and SBR.

As suggested by Wang et al., once the initial dispersion of filler is achieved through mechanical mixing, the already-dispersed filler will tend to reaggregate at elevated temperature experienced during vulcanization and annealing because the reaggregation of filler is thermodynamically favorable.⁴⁹ The reaggregation force of the filler can be determined by the difference in potential energy (ΔW_a) between the formation of a filler–filler interface and a rubber–rubber interface from two filler–rubber interfaces, which can be calculated using the equation⁴⁷

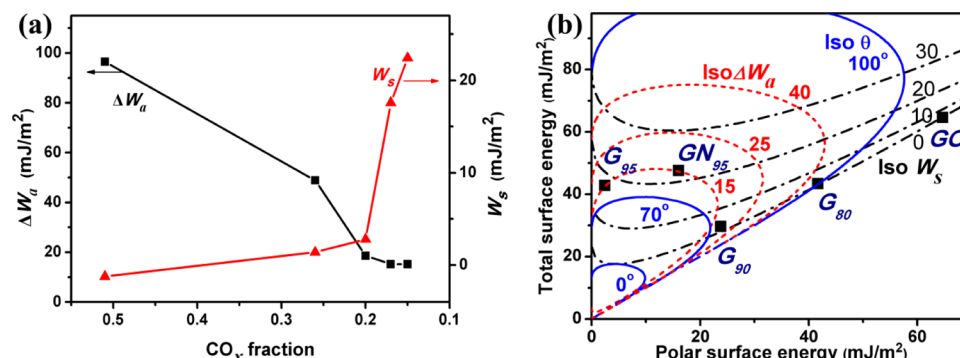


Figure 7. (a) ΔW_a and W_s as a function of CO_x fraction. (b) Plot of the total surface energy of the filler versus its polar part, with isolines for contact angle, ΔW_a , and W_s .

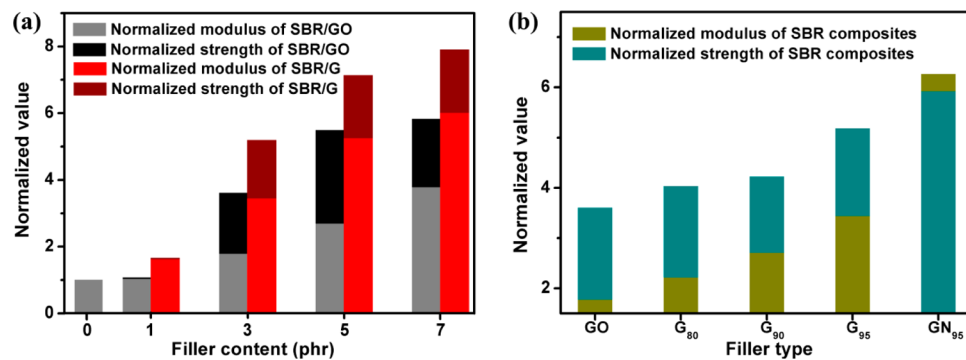


Figure 8. (a) Modulus and strength values for SBR/GO and SBR/G composites with various filler loadings, normalized to the values for neat SBR. (b) Modulus and strength values for composites containing 3 phr GO or graphene with different extents of reduction, normalized to the values for neat SBR.

$$\begin{aligned} \Delta W_a = & W_{FF} + W_{RR} - 2W_{RF} = 2(\gamma_F^d + \gamma_F^p) + 2(\gamma_R^d + \gamma_R^p) \\ & - 4(\sqrt{\gamma_R^d + \gamma_F^d} + \sqrt{\gamma_R^p + \gamma_F^p}) = 2(\sqrt{\gamma_R^d} - \sqrt{\gamma_F^d})^2 \\ & + 2(\sqrt{\gamma_R^p} - \sqrt{\gamma_F^p})^2 \end{aligned} \quad (5)$$

In eq 5, a bigger value of ΔW_a represents a greater thermodynamic driving force for the reaggregation of the filler. Besides, ΔW_a is always positive, revealing that the filler will inevitably reaggregate at elevated temperature unless the polar and dispersive components of the surface energies for the filler and rubber matrix are identical. The dependence of ΔW_a on the CO_x fraction of graphene is illustrated in Figure 7a. The value of ΔW_a is the highest for GO in SBR, suggesting that GO tends to undergo severe reaggregation because of the great discrepancy in the physicochemical surface properties of GO and SBR. Compared with GO, the values of ΔW_a for G₈₀ and G₉₀ in SBR is sharply decreased, implying that the reaggregation of graphene is suppressed. Interestingly, in the case of G₉₅ and GN₉₅, when the CO_x fraction is less than 0.2, the ΔW_a value exhibits little variation with respect to that for G₉₀ in SBR.

It is well documented that the interfacial interaction is of crucial importance in determining the properties of composites. The interfacial interaction can be reflected in the mobility of the rubber chains at the interface, which is related to the work of spreading, W_s , specifically, the difference between W_{RF} and W_{RR} :⁴⁸

$$W_s = W_{RF} - W_{RR} = 2(\sqrt{\gamma_R^d \gamma_F^d} + \sqrt{\gamma_R^p \gamma_F^p}) - 2(\gamma_R^d + \gamma_R^p) \quad (6)$$

The larger the value of W_s , the stronger attractive interaction between the filler and rubber. The dependence of W_s on the CO_x of graphene is also shown in Figure 7a. The value of W_s tends to increase with decreasing CO_x fraction, indicating that the interfacial adhesion becomes stronger as the CO_x fraction decreases. In contrast to the change trend of ΔW_a , W_s exhibits less dependence on the CO_x fraction when this fraction is greater than 0.2, whereas W_s abruptly increases with a slight decrease in CO_x fraction when the CO_x fraction is less than 0.2. Considering the dependences of W_s and ΔW_a on the CO_x fraction, we propose that a critical value of CO_x exists, perhaps 0.2. At CO_x fractions greater than this critical value, the CO_x fraction exhibits an increasingly strong effect on the dispersion of the graphene but has little effect on the interfacial adhesion. In contrast, at CO_x fractions less than this critical value, the

CO_x fraction exhibits a significant and positive effect on the interfacial adhesion but exhibits little influence on the dispersion of the graphene.

To vividly illustrate the interplay of the wetting of the filler by rubber and the work of adhesion between the rubber and filler, a so-called “wetting-envelope-adhesion plot”, as suggested previously by Heinrich et al., is presented in Figure 7b. The isolines for the contact angles, ΔW_a , and W_s within a plot of the surface energy of the filler versus its polar component can be determined by solving eqs 4–6 for SBR (i.e., γ_R^d and γ_R^p are known and γ_F^d and γ_F^p vary). The individual data points represent the surface energy of the GO or graphene. It can be seen that GO falls outside the envelope of $\theta = 100^\circ$, delivering the very poor wetting properties of GO by SBR. Upon reduction, SBR exhibits increasing wettability on the resulting graphene, especially for G₉₅ and GN₉₅. It should be pointed out that the dispersion of GO in SBR, as revealed by the TEM images, is still fairly uniform, although it is not as good as the dispersion of graphene. This paradox can be explained by the fact that the wettability calculation only considers the thermodynamic contribution but not involves the dynamics contribution. Regarding the dynamics contribution, latex mixing technology can prevent the aggregation of GO through the rapid condensation of SBR chains during the coagulation process, and the mechanical energy introduced during two-roll mill mixing can promote the breakdown of GO aggregates. On the basis of the values of ΔW_a , graphene is expected to be better dispersed than GO due to the lower ΔW_a value of graphene in SBR. In addition, G₉₀, G₉₅, and GN₉₅ fall in the nearby iso- ΔW_a line of 15, suggesting that the dispersion of graphene is almost unchanged when the CO_x fraction of graphene is less than 0.2. Regarding the value of W_s , a decrease in the CO_x fraction clearly leads to a larger value of W_s , i.e., to a stronger interfacial adhesion. More importantly, since graphene has various derivatives with different surface properties, this “wetting-envelope-adhesion plot” may provide thermodynamic guidelines to predict the dispersion, reaggregation behavior, and interfacial adhesion in various graphene derivatives filled SBR composites. Such a plot may thereby serve as a foundation for the design of graphene with an ideal surface chemistry for SBR reinforcement.

Mechanical Performance of Composites. To clearly visualize the effect of the graphene surface chemistry on the performance of the composites, the tensile strengths and moduli, which are defined as stress values at fracture and 300% strain, for all composites were normalized to the values for neat

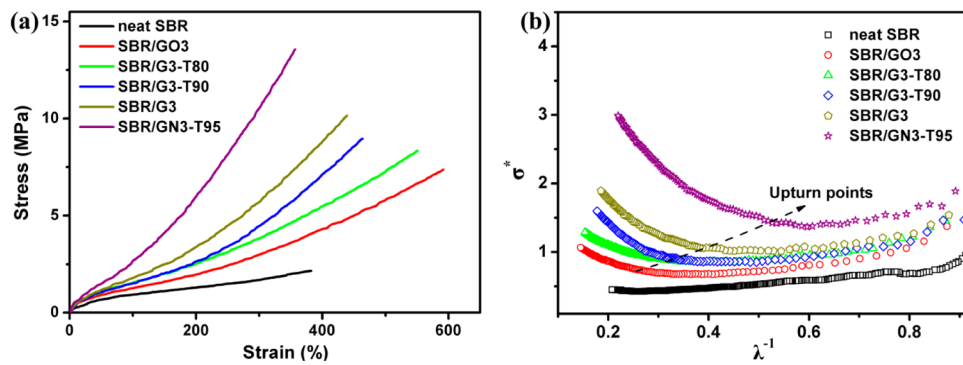


Figure 9. (a) Typical stress–strain curves of SBR composites containing 3 phr fillers. (b) σ^* as a function of λ^{-1} for SBR composites with 3 phr fillers based on the Mooney–Rivlin equation.

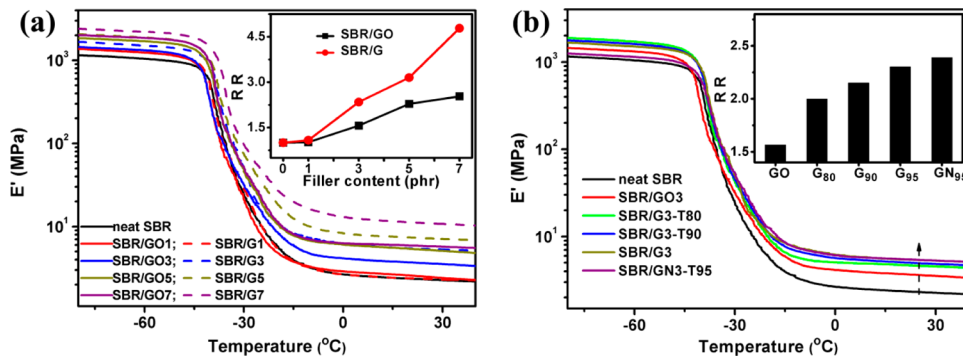


Figure 10. E' versus temperature for (a) SBR/GO and SBR/G composites and (b) SBR/graphene composites containing graphene with different reduction extent. The insets are the reinforcement ratios (RR, calculated using E' at 25 °C) for the composites with respect to neat SBR.

SBR, as presented in Figure 8. In addition, representative stress–strain curves for the composites containing graphene with different surface chemistry are compared in Figure 9a, and the stress–strain curves for the SBR/GO and SBR/G composites with various filler loadings are depicted in Figure S7. It is evident that both GO and graphene give rise to a significant increase in the modulus and ultimate strength of the composites. Notably, the SBR/G composites exhibit superior performance with respect to the SBR/GO composites. Furthermore, as shown in Figures 8b and 9a, at a given filler content of 3 phr, the moduli and strength of the composites consistently improve as the CO_x fraction of graphene decreases, which is due to the improved interfacial interaction and dispersion of graphene. In particular, with respect to neat SBR, the moduli and strength for SBR/G3 are increased by about 240% and 420%, respectively, and the moduli and strength for SBR/GN3-T95 are improved by about 530% and 490%, respectively. Such improvements are much higher than those achieved in modified-graphene filled rubber composites, suggesting that the optimized graphene surface chemistry even without functionalization can produce higher-performance composites. For example, Liu et al. incorporated sodium humate-modified graphene into carboxylated nitrile rubber, and 60% increase in moduli and 140% improvement in strength were achieved with the addition of 3 phr modified graphene.⁵⁰ Huang et al. reported that the inclusion of 3 phr silane-modified GO into NR gives rise to 320% and 90% increase in the moduli and strength, respectively.¹⁵ Even more striking, the modulus of SBR/GN3-T95 is considerably increased by approximately a factor of 2 compared with that of SBR/G3. Although the underlying mechanism accounting for such an abrupt increment remains unclear, we suggest that it may be related to the

high N-doping level in GN₉₅. As previously revealed, GN₉₅, which was obtained using ammonia and hydrazine hydrate as the reducer, exhibits a high level of N-doping. The N 1s spectrum can be deconvoluted into three peaks: pyridinic N ($-C=N$), nitrogen oxide, and quaternary N species (Figure S8).²² The $-C=N$ component, which is an efficient contributor in rubber accelerators, may participate in the rubber vulcanization reaction, thus improving the interfacial adhesion through covalent bonding.⁵¹ In addition, the strain at break of the composites decreases with increasing CO_x fraction because the strong interfacial adhesion between graphene and SBR restricts the mobility of the chains, causing the materials to break at lower strain.

The elastomeric network and the interfacial interaction can be estimated using the well-known Mooney–Rivlin equation by plotting the reduced stress (σ^*) against the reciprocal of the extension ratio (λ), following eq 7:⁵²

$$\sigma^* = \sigma / (\lambda - \lambda^{-2}) = 2C_1 + 2C_2\lambda^{-1} \quad (7)$$

where σ is the stress and $2C_1$ and $2C_2$ are constants that are independent of λ . As illustrated in Figure 9b, the σ^* of neat SBR is nearly constant, whereas the σ^* values of all composites exhibit an abrupt upturn at high λ . This upturn is attributed to the finite extensibility of polymer chains bridging neighboring filler sheets during stretching.⁵³ In the SBR composites, as the CO_x fraction of the graphene decreases, the absolute value of σ^* gradually increases and the value of λ^{-1} at which the upturn point occurs consistently increases. Such observations can be explained by the facts that the graphene can serve as physical cross-linking in the composites and that the improved dispersion of graphene and improved interfacial interaction

can promote chain orientation between two adjacent points by allowing the chains to slip along the graphene when deformation is applied.⁵² It need to point out that the filler sheets may act as physical barriers to chain mobility in unstretched composites; however, the alignment and orientation of the SBR chains can be easily realized through the slippage of the chains along the sheets upon stretching. Given that chain orientation is critical to rubber reinforcement,⁵⁴ the underlying cause for the superior mechanical properties of composites filled with graphene with a lower CO_x fraction may be a combination of the improved dispersion of the graphene, the enhanced interfacial adhesion, and the promoted chain orientation.

Figure 10 illustrates the temperature dependence of the storage moduli (E') of the composites, and the insets are the reinforcement ratios (calculated using E' at 25 °C) for the composites with respect to neat SBR. With the addition of GO or graphene, all composites exhibit increased E' and a greater reinforcement ratio with increasing filler loading. In particular, compared with SBR/GO composites, larger increases in E' are achieved in the SBR/G composites over the entire temperature range (Figure 10a). This finding can be explained by considering that the stronger interfacial interaction in the SBR/G composites ensures efficient load transfer from the matrix to filler. To further estimate the effect of the graphene surface chemistry on the properties of the composites, the E' values and reinforcement ratios of composite-filled graphene with different extents of reduction are shown in Figure 10b. As expected, graphene with a lower CO_x fraction exhibits a greater reinforcing efficiency for SBR.

4. CONCLUSIONS

SBR/graphene composites containing graphene with different and tailored surface chemistry were prepared via the *in situ* chemical reduction of GO. Dielectric relaxation spectroscopy revealed that the bulk segmental relaxation of the SBR in these composites is independent of the surface chemistry of the graphene, whereas the interfacial relaxation is retarded in composites with stronger graphene–SBR interaction. The contribution of the graphene surface chemistry to the dispersion of graphene and interfacial adhesion was quantified by measuring the surface energy of the graphene. These results led to the conclusion that a critical value of the CO_x fraction in the graphene exists, perhaps 0.2. At CO_x fractions greater than 0.2, this fraction has an increasingly strong effect on the dispersion of graphene, whereas below 0.2, the CO_x fraction exerts a significant and positive effect on the interfacial adhesion. Graphene with a lower CO_x fraction can be more easily dispersed in the composite and exhibits stronger interfacial adhesion with the SBR matrix, resulting in greater enhancement on the mechanical properties of the composite. In addition, the presence of N-doping in the graphene may play an important role in improving the interfacial adhesion between the graphene and SBR matrix. The present work is expected to provide significant insight into the relationships between the surface chemistry of the graphene and structures (interfacial adhesion and graphene dispersion) as well as mechanical properties of the composites; this insight provides a foundation for the preparation of high-performance rubber/graphene composites from the perspective of the rational design of graphene surface chemistry.

ASSOCIATED CONTENT

Supporting Information

XPS analysis for GO and graphene samples, additional SEM images for the composites, ML and MH for the composites, dielectric loss M'' for SBR/G3-T80 as a function of frequency, dielectric loss spectra of SBR/GO3, SBR/G3, and SBR/GN3-T95 composites, typical stress–strain curves for SBR/GO and SBR/G composites. This material is available free of charge via the Internet at <http://pubs.acs.org>.

AUTHOR INFORMATION

Corresponding Author

*E-mail: psbcguo@scut.edu.cn (B.G.).

Notes

The authors declare no competing financial interest.

ACKNOWLEDGMENTS

This work was supported by National Basic Research Program of China (2015CB654703), National Natural Science Foundation of China (51222301, 51221002, and 51320105012), and Fundamental Research Project for the Central Universities (2014ZG0001).

REFERENCES

- (1) Valentin, J. L.; Mora-Barrantes, I.; Carretero-Gonzalez, J.; Lopez-Manchado, M. A.; Sotta, P.; Long, D. R.; Saalwachter, K. *Macromolecules* **2010**, *43*, 334–346.
- (2) Hamed, G. R. *Rubber Chem. Technol.* **2000**, *73*, 524–533.
- (3) Leblanc, J. L. *Prog. Polym. Sci.* **2002**, *27*, 627–687.
- (4) Kohls, D. J.; Beaucage, G. *Curr. Opin. Solid State Mater. Sci.* **2002**, *6*, 183–194.
- (5) Huang, X.; Qi, X.; Boey, F.; Zhang, H. *Chem. Soc. Rev.* **2012**, *41*, 666–686.
- (6) Potts, J. R.; Shankar, O.; Du, L.; Ruoff, R. S. *Macromolecules* **2012**, *45*, 6045–6055.
- (7) Tang, Z.; Wu, X.; Guo, B.; Zhang, L.; Jia, D. *J. Mater. Chem.* **2012**, *22*, 7492–7501.
- (8) Khan, U.; May, P.; O'Neill, A.; Coleman, J. N. *Carbon* **2010**, *48*, 4035.
- (9) Kuilla, T.; Bhadra, S.; Yao, D. H.; Kim, N. H.; Bose, S.; Lee, J. H. *Prog. Polym. Sci.* **2010**, *35*, 1350–1375.
- (10) Sadasiyuni, K. K.; Ponnamma, D.; Thomas, S.; Grohens, Y. *Prog. Polym. Sci.* **2014**, *39*, 749–780.
- (11) Kang, H. L.; Zuo, K. H.; Wang, Z.; Zhang, L. Q.; Liu, L.; Guo, B. C. *Compos. Sci. Technol.* **2014**, *92*, 1–8.
- (12) Li, Y.; Wang, Q.; Wang, T.; Pan, G. *J. Mater. Sci.* **2012**, *47*, 730–738.
- (13) Li, Z.; Young, R. J.; Wang, R.; Yang, F.; Hao, L.; Jiao, W.; Liu, W. *Polymer* **2013**, *54*, 5821–5829.
- (14) Mao, Y.; Wen, S.; Chen, Y.; Zhang, F.; Panine, P.; Chan, T. W.; Zhang, L.; Liang, Y.; Liu, L. *Sci. Rep.* **2013**, *3*, 2508.
- (15) Wu, J.; Huang, G.; Li, H.; Wu, S.; Liu, Y.; Zheng, J. *Polymer* **2013**, *54*, 1930–1937.
- (16) Hernández, M.; Bernal, M. d. M.; Verdejo, R.; Ezquerra, T. A.; López-Manchado, M. A. *Compos. Sci. Technol.* **2012**, *73*, 40–46.
- (17) Zhan, Y.; Wu, J.; Xia, H.; Yan, N.; Fei, G.; Yuan, G. *Macromol. Mater. Eng.* **2011**, *296*, 590–602.
- (18) Ramanathan, T.; Abdala, A. A.; Stankovich, S.; Dikin, D. A.; Herrera-Alonso, M.; Piner, R. D.; Adamson, D. H.; Schniepp, H. C.; Chen, X.; Ruoff, R. S.; Nguyen, S. T.; Aksay, I. A.; Prud'homme, R. K.; Brinson, L. C. *Nat. Nanotechnol.* **2008**, *3*, 327–331.
- (19) Tang, Z.; Kang, H.; Shen, Z.; Guo, B.; Zhang, L.; Jia, D. *Macromolecules* **2012**, *45*, 3444–3451.
- (20) Rooj, S.; Das, A.; Stockelhuber, K. W.; Wang, D. Y.; Galiatsatos, V.; Heinrich, G. *Soft Matter* **2013**, *9*, 3798–3808.

- (21) Long, D.; Li, W.; Ling, L.; Miyawaki, J.; Mochida, I.; Yoon, S. H. *Langmuir* **2010**, *26*, 16096–102.
- (22) Hwang, J. O.; Park, J. S.; Choi, D. S.; Kim, J. Y.; Lee, S. H.; Lee, K. E.; Kim, Y. H.; Song, M. H.; Yoo, S.; Kim, S. O. *ACS Nano* **2012**, *6*, 159–167.
- (23) Kudin, K. N.; Ozbas, B.; Schniepp, H. C.; Prud'Homme, R. K.; Aksay, I. A.; Car, R. *Nano Lett.* **2008**, *8*, 36–41.
- (24) Stankovich, S.; Dikin, D. A.; Piner, R. D.; Kohlhaas, K. A.; Kleinhammes, A.; Jia, Y.; Wu, Y.; Nguyen, S. T.; Ruoff, R. S. *Carbon* **2007**, *45*, 1558–1565.
- (25) Kim, H.; Abdala, A. A.; Macosko, C. W. *Macromolecules* **2010**, *43*, 6515–6530.
- (26) Da Costa, H. M.; Nunes, R. C. R.; Visconte, L. L. Y.; Furtado, C. R. G. *Kautsch. Gummi Kunstst.* **2001**, *54*, 242–249.
- (27) Haseena, A. P.; Dasan, K. P.; Namitha, R.; Unnikrishnan, G.; Thomas, S. *Compos. Interfaces* **2004**, *11*, 489–513.
- (28) Berriot, J.; Lequeux, F.; Montes, H.; Pernot, H. *Polymer* **2002**, *43*, 6131–6138.
- (29) Hashim, A. S.; Azahari, B.; Ikeda, Y.; Kohjiya, S. *Rubber Chem. Technol.* **1998**, *71*, 289–299.
- (30) Robertson, C. G.; Lin, C. J.; Rackaitis, M.; Roland, C. M. *Macromolecules* **2008**, *41*, 2727–2731.
- (31) Robertson, C. G.; Roland, C. M. *Rubber Chem. Technol.* **2008**, *81*, 506–522.
- (32) Tang, Z.; Wei, Q.; Lin, T.; Guo, B.; Jia, D. *RSC Adv.* **2013**, *3*, 17057–17064.
- (33) Tian, M.; Cheng, L.; Zhang, L. *J. Appl. Polym. Sci.* **2008**, *110*, 262–269.
- (34) Lei, Y.; Tang, Z.; Zhu, L.; Guo, B.; Jia, D. *Polymer* **2011**, *52*, 1337–1344.
- (35) Vo, L. T.; Anastasiadis, S. H.; Giannelis, E. P. *Macromolecules* **2011**, *44*, 6162–6171.
- (36) Wu, S.; Tang, Z.; Guo, B.; Zhang, L.; Jia, D. *RSC Adv.* **2013**, *3*, 14549–14559.
- (37) Mijovic, J.; Lee, H. K.; Kenny, J.; Mays, J. *Macromolecules* **2006**, *39*, 2172–2182.
- (38) Hernandez, M.; Carretero-Gonzalez, J.; Verdejo, R.; Ezquerra, T. A.; Lopez-Manchado, M. A. *Macromolecules* **2010**, *43*, 643–651.
- (39) Meier, J. G.; Kluppel, M. *Macromol. Mater. Eng.* **2008**, *293*, 38–38.
- (40) Kim, B.; Lee, J.; Yu, I. S. *J. Appl. Phys.* **2003**, *94*, 6724–6728.
- (41) Mamunya, Y. P.; Levchenko, V. V.; Rybak, A.; Boiteux, G.; Lebedev, E. V.; Ulanksi, J.; Seytre, G. *J. Non-Cryst. Solids* **2010**, *356*, 635–641.
- (42) Chakraborty, G.; Meikap, A. K.; Babu, R.; Blau, W. J. *Solid State Commun.* **2011**, *151*, 754–758.
- (43) Stockelhuber, K. W.; Svistkov, A. S.; Pelevin, A. G.; Heinrich, G. *Macromolecules* **2011**, *44*, 4366–4381.
- (44) Natarajan, B.; Li, Y.; Deng, H.; Brinson, L. C.; Schadler, L. S. *Macromolecules* **2013**, *46*, 2833–2841.
- (45) Fowkes, F. M. *J. Phys. Chem.* **1963**, *67*, 2538–2541.
- (46) Wang, S. R.; Zhang, Y.; Abidi, N.; Cabrales, L. *Langmuir* **2009**, *25*, 11078–11081.
- (47) Breneman, C. M.; Brinson, L. C.; Schadler, L. S.; Natarajan, B.; Krein, M.; Wu, K.; Morkowchuk, L.; Li, Y.; Deng, H.; Xu, H. Y. *Adv. Funct. Mater.* **2013**, *23*, 5746–5752.
- (48) Stockelhuber, K. W.; Das, A.; Jurk, R.; Heinrich, G. *Polymer* **2010**, *51*, 1954–1963.
- (49) Wolff, S.; Wang, M. J. *Rubber Chem. Technol.* **1992**, *65*, 329–342.
- (50) Liu, X.; Sun, D.; Wang, L.; Guo, B. *Ind. Eng. Chem. Res.* **2013**, *52*, 14592–14600.
- (51) Wu, J.; Xing, W.; Huang, G.; Li, H.; Tang, M.; Wu, S.; Liu, Y. *Polymer* **2013**, *54*, 1930–1937.
- (52) Bokobza, L.; Erman, B. *Macromolecules* **2000**, *33*, 8858–8864.
- (53) Joly, S.; Garnaud, G.; Ollitrault, R.; Bokobza, L.; Mark, J. *Chem. Mater.* **2002**, *14*, 4202–4208.
- (54) Wang, Z.; Liu, J.; Wu, S.; Wang, W.; Zhang, L. *Phys. Chem. Chem. Phys.* **2010**, *12*, 3014–3030.